

Optoelectronic analysis of multijunction wire array solar cells

Daniel B. Turner-Evans, Christopher T. Chen, Hal Emmer, William E. McMahon, and Harry A. Atwater

Citation: *J. Appl. Phys.* **114**, 014501 (2013); doi: 10.1063/1.4812397

View online: <http://dx.doi.org/10.1063/1.4812397>

View Table of Contents: <http://jap.aip.org/resource/1/JAPIAU/v114/i1>

Published by the AIP Publishing LLC.

Additional information on J. Appl. Phys.

Journal Homepage: <http://jap.aip.org/>

Journal Information: http://jap.aip.org/about/about_the_journal

Top downloads: http://jap.aip.org/features/most_downloaded

Information for Authors: <http://jap.aip.org/authors>

ADVERTISEMENT

The advertisement banner for AIP Advances features a light green background with abstract, flowing, wavy lines in a darker green shade. The AIP Advances logo is prominently displayed in the center, with 'AIP' in blue and 'Advances' in green. To the right of the logo is a circular seal with the text 'Now Indexed in Thomson Reuters Databases'. Below the logo, the text 'Explore AIP's open access journal:' is followed by a list of three bullet points: 'Rapid publication', 'Article-level metrics', and 'Post-publication rating and commenting'.

AIPAdvances

Now Indexed in Thomson Reuters Databases

Explore AIP's open access journal:

- Rapid publication
- Article-level metrics
- Post-publication rating and commenting

Optoelectronic analysis of multijunction wire array solar cells

Daniel B. Turner-Evans,^{1,a)} Christopher T. Chen,¹ Hal Emmer,¹ William E. McMahon,² and Harry A. Atwater¹

¹*Thomas J. Watson Laboratories of Applied Physics, California Institute of Technology, Pasadena, California 91125, USA*

²*National Renewable Energy Laboratory, Golden, Colorado 80401, USA*

(Received 25 April 2013; accepted 10 June 2013; published online 2 July 2013)

Wire arrays have demonstrated promising photovoltaic performance as single junction solar cells and are well suited to defect mitigation in heteroepitaxy. These attributes can combine in tandem wire array solar cells, potentially leading to high efficiencies. Here, we demonstrate initial growths of GaAs on $\text{Si}_{0.9}\text{Ge}_{0.1}$ structures and investigate III-V on $\text{Si}_{1-x}\text{Ge}_x$ device design with an analytical model and optoelectronic simulations. We consider $\text{Si}_{0.1}\text{Ge}_{0.9}$ wires coated with a $\text{GaAs}_{0.9}\text{P}_{0.1}$ shell in three different geometries: conformal, hemispherical, and spherical. The analytical model indicates that efficiencies approaching 34% are achievable with high quality materials. Full field electromagnetic simulations serve to elucidate the optical loss mechanisms and demonstrate light guiding into the wire core. Simulated current-voltage curves under solar illumination reveal the impact of a varying $\text{GaAs}_{0.9}\text{P}_{0.1}$ minority carrier lifetime. Finally, defective regions at the hetero-interface are shown to have a negligible effect on device performance if highly doped so as to serve as a back surface field. Overall, the growths and the model demonstrate the feasibility of the proposed geometries and can be used to guide tandem wire array solar cell designs.

© 2013 AIP Publishing LLC. [<http://dx.doi.org/10.1063/1.4812397>]

I. INTRODUCTION

A. Background

Wire array solar cells have the potential to significantly reduce overall installed module costs by providing a lightweight, flexible architecture that can be readily mounted on rooftops and by using less material than conventional cell designs while achieving comparable efficiencies. Towards this end, single junction Si, CdS, InP, or GaAs wire array solar cells have been synthesized and have demonstrated respectable photovoltaic performance.^{1–12} Furthermore, Si wire array cells, though grown on a rigid, expensive substrate, can be embedded in a flexible polymer and peeled off, allowing the substrate to be reused for further growths.^{13,14} The peeled off arrays still absorb up to 96% of the incident light despite using 100 times less material than a comparable planar Si cell.² Si wire array devices have reached efficiencies of 2–3% in liquid electrolyte¹⁵ and of up to 8% in large-area wire array solar cells,⁴ and single wire measurements reveal that large area array efficiencies of greater than 17% are possible.³ Finally, InP nanowire array cells have recently demonstrated a light conversion efficiency of 13.8%.¹² Thus, high performance single junction wire array cells are rapidly becoming a proven technology.

B. Multijunction material selection

Multijunction arrays offer the advantages of wire array solar cells along with both higher efficiencies and higher voltages. The latter is especially attractive for photoelectrochemical solar fuel cells where the minimum voltage

required for water splitting exceeds 1.23 V. Along these lines, GaP/Si wire heterostructures have been fabricated as potential solar fuel devices.¹⁶ However, in order to obtain high efficiencies for solar electricity generation, different constituent materials must be selected; the limiting efficiency for a GaP/Si combination is less than that of a single junction Si cell alone due to severe current limiting by the GaP subcell. Thus, to achieve a high efficiency device, the bandgaps of the constituent materials must be chosen so that the photocurrent in each layer is matched. Additionally, mismatch strain relieving dislocations can act as recombination centers and thus lattice-matched material systems are desirable, though recent work suggests that the wire geometry may facilitate high quality growth of lattice mismatched materials.¹⁷ When growing epitaxial layers on wires, dislocations due to lattice mismatch can be forced to propagate radially outward from the wire interface, allowing high quality material to be grown axially.

Careful consideration of the detailed balance efficiencies for dual junction, series connected devices combined with the constraint of lattice matching reveal that $\text{Si}_{0.1}\text{Ge}_{0.9}$, $\text{GaAs}_{0.9}\text{P}_{0.1}$ and $\text{Ga}_{0.56}\text{In}_{0.44}\text{P}$ are an almost ideal material system for the core, shell, and window layers of a tandem wire array device. The combination has a detailed balance efficiency of over 40% (see Supplemental material²⁵). The $\text{Ga}_{0.56}\text{In}_{0.44}\text{P}$, the $\text{GaAs}_{0.9}\text{P}_{0.1}$, and the $\text{Si}_{0.1}\text{Ge}_{0.9}$ bandgaps are 1.97, 1.54, and 0.79 eV, respectively. Also of note, despite the specific composition choice, the chosen material combination is somewhat flexible; the limiting efficiency is well over 35% across a broad range of alloys. Practically, $\text{Si}_{1-x}\text{Ge}_x$ wires have been successfully synthesized¹⁸ and both Si and Ge wires can be grown using high temperature chlorosilane chemistry,¹⁹ which has been demonstrated to produce high fidelity, ordered arrays.²⁰

^{a)}Author to whom correspondence should be addressed. Electronic mail: dt@caltech.edu

C. Structure geometry

If the $\text{GaAs}_{0.9}\text{P}_{0.1}$ top cell first fully absorbs all of the available above bandgap photons from the solar spectrum and the $\text{Si}_{0.1}\text{Ge}_{0.9}$ bottom cell then absorbs all of the remaining photons above its bandgap, each will contribute $\sim 28 \text{ mA/cm}^2$ of current. Thus, in order to achieve current matching, the incident light must first pass through the $\text{GaAs}_{0.9}\text{P}_{0.1}$ and the optical path length must be long enough in the $\text{GaAs}_{0.9}\text{P}_{0.1}$ so that all of the above bandgap photons are absorbed. Combining this constraint with realistic growth geometries led to the three device designs depicted in Fig. 1. In the conformal structure, the III-V layers are deposited directly on a p-n $\text{Si}_{0.1}\text{Ge}_{0.9}$ radial junction wire array. In the hemisphere structure, the $\text{Si}_{0.1}\text{Ge}_{0.9}$ wire array is infilled with a dielectric material and growth of the III-V layers is then templated from the wire tips, in a method analogous to epitaxial lateral overgrowth. The ellipsoidal structures allow for a close packed array of $\text{GaAs}_{0.9}\text{P}_{0.1}$ absorbers at the top of the cell, directing all incident light through the $\text{GaAs}_{0.9}\text{P}_{0.1}$ material before it reaches the $\text{Si}_{0.1}\text{Ge}_{0.9}$. Finally, in the sphere structure, the wire sidewalls are protected by a dielectric, and III-V growth proceeds in all directions from the seed region near the top of the wire. Again, the $\text{GaAs}_{0.9}\text{P}_{0.1}$ ellipsoids are close packed.

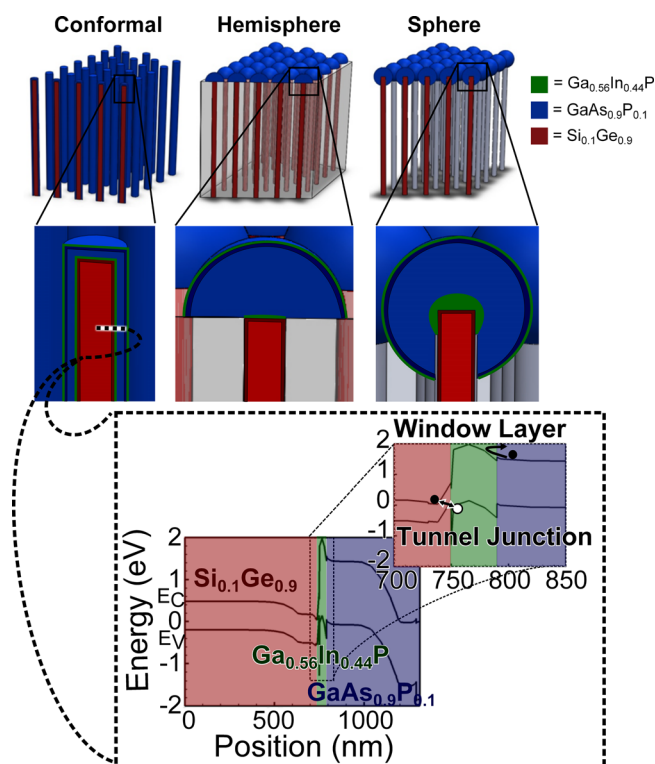


FIG. 1. Overview of the multijunction wire array geometries and electronic structure. (Top) The three architectures under consideration. The window layers, top cell, and bottom cell are colored green, blue, and red, respectively. For the $\text{GaAs}_{0.9}\text{P}_{0.1}$ top cell and the $\text{Si}_{0.1}\text{Ge}_{0.9}$ bottom cell, the darker and lighter areas symbolize the n-type and p-type regions. (Bottom) A representative band diagram with the $\text{Si}_{0.1}\text{Ge}_{0.9}$ and $\text{GaAs}_{0.9}\text{P}_{0.1}$ p-n junctions and the $\text{Ga}_{0.56}\text{In}_{0.44}\text{P}$ tunnel junction and window layers. The 20 nm of $\text{Si}_{0.1}\text{Ge}_{0.9}$ closest to the $\text{Ga}_{0.56}\text{In}_{0.44}\text{P}$ is highly doped to serve as part of a tunnel junction and hence experiences bandgap narrowing.

An example of GaAs growth on $\text{Si}_{0.9}\text{Ge}_{0.1}$ in the sphere geometry can be seen in Fig. 2. The alloys are not the same composition as those desired above, but they serve as a representative example. A $\text{Si}_{0.9}\text{Ge}_{0.1}$ wire array was grown on a Si substrate through a vapor-liquid-solid chlorosilane process, cleaned, and coated with plasma enhanced chemical vapor deposited SiO_x . The array was then infilled with mounting wax (Quickstick 135, South Bay Tech.) and the wire tips exposed through O plasma ashing. The SiO_x was removed with buffered hydrofluoric acid before removing the wax with acetone. Finally, GaAs was grown on the exposed tips after being seeded with $\text{GaAs/Ga}_{0.8}\text{Al}_{0.2}\text{As}$ buffer layers. The x-ray diffraction rocking curve reveals the presence of the Si growth substrate, $\text{Si}_{0.9}\text{Ge}_{0.1}$ wires, and GaAs shells. Future reports will delve extensively into the material and electronic properties of $\text{GaAs}_x\text{P}_{1-x}/\text{Si}_{1-x}\text{Ge}_x$ heterostructures in all three geometries, but the remainder of this manuscript will focus on the design considerations and potential efficiencies of such devices.

II. ANALYTICAL MODEL: HEMISPHERICAL CASE

While not as accurate as finite element numerical simulations, a simplified analytical model allows for physical insight and rapid exploration of the device parameters. An analytical model for the conformal wire array device geometry may be solved by extension of the model of Kayes *et al.* and is not covered here.²¹ Instead, the hemisphere design was chosen as a case study. The spherical design can be solved through a similar analytical approach, though the absorption profile should be modified. For the hemisphere, the optical absorption and current-voltage curves were calculated for a variety of geometries, materials, and recombination parameters. Optical constants for the $\text{Si}_{0.1}\text{Ge}_{0.9}$ were taken from Palik.²² Constants for the $\text{GaAs}_{0.9}\text{P}_{0.1}$ were generated by shifting GaAs n and κ vs. energy values by a constant energy such that κ fell to 0 at the desired bandgap. Electronic material parameters were taken from a database made available by the Ioffe Institute.²³ A window layer was not explicitly incorporated. Rather, the surface

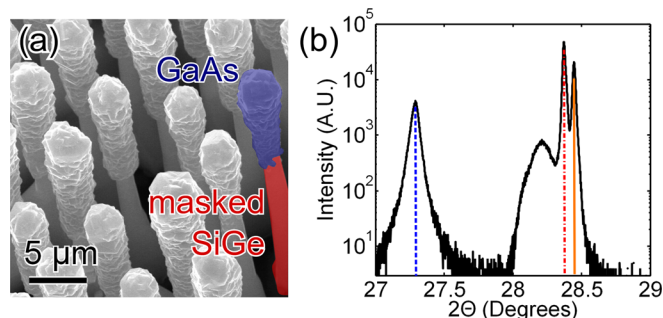


FIG. 2. MOCVD growth of GaAs on $\text{Si}_{0.9}\text{Ge}_{0.1}$ wires. (a) SEM of GaAs grown on SiO_x masked $\text{Si}_{0.9}\text{Ge}_{0.1}$ wires. The wires, in turn, are grown on a Si substrate. (b) XRD rocking curve of the structures shown in (a). The GaAs peak is indicated with the dotted blue line. $\text{Si}_{0.9}\text{Ge}_{0.1}$ is marked with the red dash-dotted line. The Si peak falls on the orange solid line. The unmarked peak is likely $\text{Si}_x\text{Ge}_{1-x}$ undergrowth on the Si substrate.

recombination velocity (SRV) at the inner and outer GaAs_{0.9}P_{0.1} surfaces was directly altered.

A. Optical model

First, we solved for the III-V top subcell performance. The optical absorption profile of the III-V layers was calculated by considering the excitation of a sphere of material by a plane wave, using Mie theory.²⁴ The absorption at each wavelength was evaluated, weighted by the solar spectrum, and summed to yield an optical generation profile. The absorption profile was found to be similar to an exponentially attenuated Beer-Lambert profile, as might be expected for direct gap GaAs_{0.9}P_{0.1}. Photons are absorbed before they can fully occupy the modes of the structure. Thus, a Beer Lambert photogeneration profile was assumed in the device physics equations in order to make them analytically tractable.²⁵

B. Device physics model

In addition to the Beer Lambert absorption assumption, the device physics model of the III-V hemisphere relied on three additional assumptions:

- (1) Transport occurs only in the radial direction.
- (2) The p-n junction is abrupt.
- (3) All of the carriers that are generated in the depletion region are collected.

With these assumptions and following the conventions outlined in Fig. 3, the limits of the depletion region may be found by maintaining charge conservation and by solving Poisson's equation in spherical coordinates, which leads to

$$V_{bi} + V = \frac{qd_2^2 N_A}{6\epsilon} + \frac{q}{3\epsilon d_2} (N_A x_4^3 + N_D x_2^3) + \frac{q}{2\epsilon} (-N_A x_4^2 + N_D x_2^2), \quad (1)$$

where $V_{bi} = \frac{kT}{q} \ln(\frac{N_A N_D}{n_i^2})$ is the built in voltage, V is the applied voltage, N_A is the p-type dopant density, N_D is the n-type dopant density, n_i is the intrinsic carrier concentration, T is the temperature, k is Boltzmann's constant, q is the fundamental electrical charge, and ϵ is the dielectric constant.

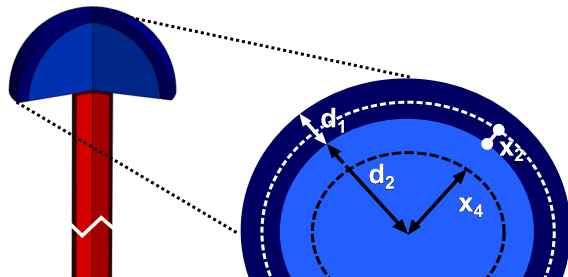


FIG. 3. Cross section of the GaAs_{0.9}P_{0.1} hemispherical shell showing the parameters used in the analytical model. The depletion region boundaries are marked with dotted lines. d_1 and d_2 are the thicknesses of the n-type and p-type regions, respectively. x_4 is the p-type quasineutral region thickness and x_2 is the n-type depletion region thickness.

Since assumption number 3 states that all of the charge carriers in the depletion region are collected,

$$J_s^{dep} = \sum_{\omega} q \Gamma_0(\omega) \frac{d_2^2}{(d_1 + d_2)^2} (\exp(\alpha(\omega)(x_2 - d_1)) - \exp(\alpha(\omega)(x_4 - d_1 - d_2))), \quad (2)$$

and from the model of Sah *et al.*²⁶ for recombination,

$$J_r^{dep} = -q U_{max} \frac{r_2(V)^3 - r_1(V)^3}{3(d_1 + d_2)^2}, \quad (3)$$

where $\Gamma_0(\omega)$ is the incident photon flux, $\alpha(\omega) = 2\omega\kappa$ is the Beer-Lambert attenuation coefficient, κ is the imaginary part of the index of refraction, $U_{max} = \frac{n_i}{\sqrt{\epsilon_{n,0}\tau_{p,0}}} \sinh(\frac{qV}{2kT})$ is the maximum recombination rate of a mid-level trap, τ is the lifetime in the n or p-type region, $r_1(V) = r(V) - L_C$, $r_2(V) = r(V) + L_C$, $r(V) = x_4 + \frac{\ln(\frac{N_A}{n_i})}{\ln(\frac{N_A N_D}{n_i^2})} (x_2 + (d_2 - x_4))$

is the point where the Fermi level crosses midgap, and $L_C = \frac{\pi kT}{2qE} = \frac{\pi kT(x_2 + (d_2 - x_4))}{2q(V_{bi} + V)}$ is the recombination collection length.

In the two quasi-neutral regions, we must solve the diffusion equation in spherical coordinates. The current may then be found from the relation $J = qD_{n,p} \frac{dn,p}{dr}$, where n, p refer to the minority carrier concentration in the region of interest and the current is evaluated at the depletion region boundaries. The boundary conditions are

$$\begin{aligned} n(0) &= \text{finite}, \\ S_n \cdot n(0) &= -D_n \frac{dn}{dr} \Big|_0, \\ n(x_4) &= n_0(e^{qV/kT} - 1), \\ p(d_2 + x_2) &= p_0(e^{qV/kT} - 1), \\ S_p \cdot p(d_1 + d_2) &= -D_p \frac{dp}{dr} \Big|_{d_1+d_2}, \end{aligned} \quad (4)$$

where S_n and S_p are the electron and hole SRVs, respectively.

In the n-type emitter, the differential equation can be solved to give

$$\begin{aligned} p &= A \frac{e^{r/L_p}}{r} + B \frac{e^{-r/L_p}}{r} + e^{\alpha(r-(d_1+d_2))} \frac{\alpha \Gamma_0}{D_p} \left(\frac{L_p^2}{1 - \alpha^2 L_p^2} \right) \\ &\times \left(1 + \frac{2\alpha L_p^2}{r(1 - \alpha^2 L_p^2)} \right), \end{aligned} \quad (5)$$

where A and B are constants to be determined from the boundary conditions.

The solution takes the same form in the p-type core (with n substituted for p), but an additional term, $\Delta \frac{\sinh(r/L_n)}{r/L_n}$, where Δ is a constant, must be included to account for the additional boundary condition. L'Hospital's rule may be used to solve for the limits at $r = 0$ and combined with the boundary conditions to find the constants.

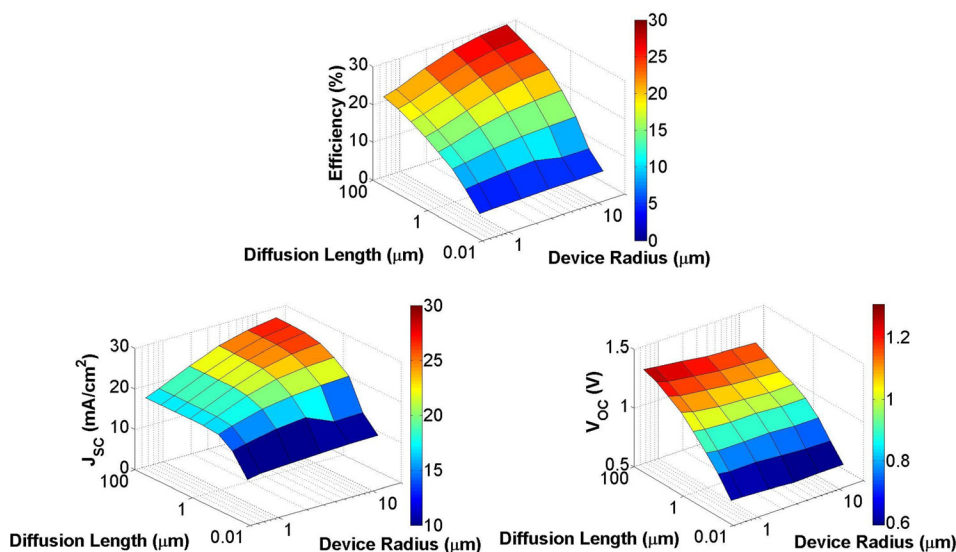


FIG. 4. Efficiency, short circuit current density, and open circuit voltage of hemispherical $\text{GaAs}_{0.9}\text{P}_{0.1}$ solar cell structures as a function of device radius and diffusion length.

C. Model results

Device characteristics for III–V hemispherical top subcells with varying radii and diffusion lengths are shown in Fig. 4. Diffusion lengths of less than 100 nm have been seen for GaP/Si wire heterostructures,¹⁶ but lengths of a few microns are regularly achieved for high quality GaAs and hence a diffusion length range of 10 nm–100 μm was explored.²⁷ The n-type emitter was set to be 100 nm thick with a dopant density of $9 \times 10^{17} \text{ cm}^{-3}$. The p-type base was doped at $5 \times 10^{16} \text{ cm}^{-3}$. Finally, the SRVs were set to 100 cm/s. The V_{OC} is relatively invariant of device diameter, but falls off uniformly with device diffusion length. The J_{SC} , on the other hand, is relatively insensitive to diffusion length until the diffusion length approaches the physical dimensions of the device. At this point, the excited carriers recombine before reaching the junction to be collected. Overall, for the parameter space surveyed, a maximum efficiency of 29.7% was achieved for a 10 μm thick device with a 100 μm diffusion length. Higher efficiencies would be possible with larger radii, but fall outside of the scope of the architectures considered herein. Also of note, the top subcells are relatively insensitive to surface recombination velocity. As the radius goes up, the surface to volume ratio goes down, and a sphere is already the shape with minimum surface-to-volume ratio. The model suggests that surface recombination velocities of

$\sim 10\,000 \text{ cm/s}$ could be tolerated with minimal effect on device performance.²⁵

Next, the hemispherical top subcell was coupled with the wire model of Kayes *et al.*²¹ to simulate current voltage curves for tandem solar cell structures. First, current-voltage curves were generated for the hemisphere and for a $\text{Si}_{0.1}\text{Ge}_{0.9}$ wire. Kirchhoff's circuit laws were then enforced for the two devices in series. Fig. 5 shows the evolution of device performance as the dimensions are altered, and Table I displays the V_{OC} , J_{SC} , efficiency, and fill factor for the devices.

The combined performance is primarily limited by the short circuit current density of the $\text{Si}_{0.1}\text{Ge}_{0.9}$ wire cell, with current matching only achieved by making the $\text{GaAs}_{0.9}\text{P}_{0.1}$ layer small enough to allow some of the blue light to reach the $\text{Si}_{0.1}\text{Ge}_{0.9}$ wire and to be absorbed therein or by making the $\text{Si}_{0.1}\text{Ge}_{0.9}$ wire much longer. $\text{Si}_{0.1}\text{Ge}_{0.9}$ is a very poor absorber in the infrared and hence the current is 2–4 mA/cm^2 lower than possible. As the wire is made longer to absorb more of the incident light, the recombination losses rise, and the wire efficiency begins to drop due to voltage losses, limiting the gains beyond a certain point. However, while the model of Kayes *et al.* assumes Beer Lambert absorption,²¹ experimental studies have demonstrated enhanced absorption in wire arrays,^{1,2} and hence higher efficiencies may be possible in real devices.

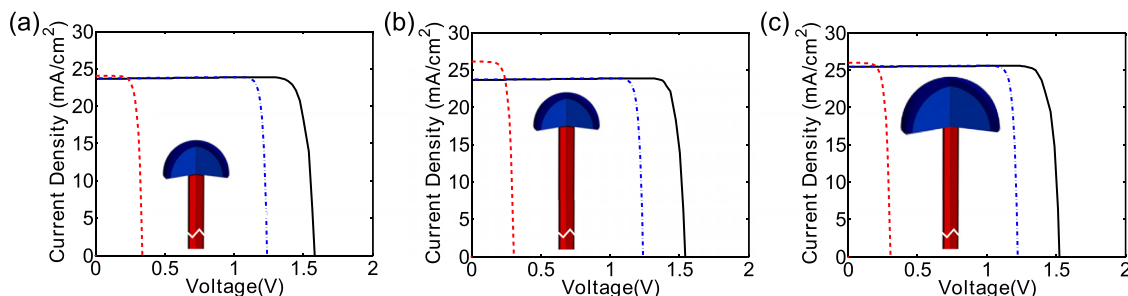


FIG. 5. Light IV curves of the $\text{Si}_{0.1}\text{Ge}_{0.9}$ wire (red dashed), the $\text{GaAs}_{0.9}\text{P}_{0.1}$ hemisphere (blue dotted-dashed), and the tandem combination (black solid) as the structure geometry is varied. In (a), the hemisphere has a 3 μm radius and the wire is 100 μm long. In (b), the wire length is increased to 400 μm . In (c), the radius is increased to 5 μm and the length is 400 μm .

TABLE I. Light IV characteristics for subcells and tandem cell as the geometry of the shell and wire are varied.

	V_{OC} (V)	J_{SC} (mA/cm ²)	Efficiency (%)	FF (%)
3 μ m GaAs _{0.9} P _{0.1} shell	1.24	23.7	26.7	90.7
100 μ m Si _{0.1} Ge _{0.9} wire	0.33	24.0	5.94	73.9
Tandem	1.57	23.6	32.4	87.1
5 μ m GaAs _{0.9} P _{0.1} shell	1.23	25.5	28.2	90.1
400 μ m Si _{0.1} Ge _{0.9} wire	0.30	26.0	5.62	71.7
Tandem	1.52	25.4	33.6	86.7

Finally, the above model assumed a perfect tunnel junction between the two subcells. However, real devices will experience a finite, though hopefully small, voltage drop across the tunnel junction. Thus, a series resistance was added to the model to account for these losses. For the first cell considered in Table I, as long as the series resistance for the tunnel junction is kept at or below $0.7 \Omega \text{ cm}^2$, the tandem efficiency will remain above 32%. For the second cell, the efficiency will remain above 33% for a resistance of up to $1 \Omega \text{ cm}^2$.²⁵

III. SIMULATIONS: CONFORMAL, HEMISPHERICAL, AND SPHERICAL CASES

A. Optical modeling

In order to create a more realistic model of all three structures, full optoelectronic finite element simulations were conducted. For each of the three geometries, a $1.5 \mu\text{m}$ diameter, $40 \mu\text{m}$ long Si_{0.1}Ge_{0.9} wire served as the base and a square array of varying pitch was assumed. Simulations of longer wires were not possible due to memory constraints. Additionally, a Ga_{0.56}In_{0.44}P window was now included. The location of each of the layers can be seen in Fig. 1. In the conformal structure, the GaAs_{0.9}P_{0.1} shell and the Ga_{0.56}In_{0.44}P layers were set to be 500 nm and 20 nm thick, respectively. In the hemispherical and spherical structures, the III–V semiconductor shell was ellipsoidal, depicting a case in which growth nucleates simultaneously at the sides and the top of the wire and continues outward. In both of these cases, the shell thickness was set such that a 500 nm gap was left between adjacent wires.

First, full field optical simulations were run using the finite difference time domain method with plane wave incident illumination.²⁸ Optical constants for Si_{0.1}Ge_{0.9} and GaAs_{0.9}P_{0.1} were found as mentioned in Sec. II, and Ga_{0.56}In_{0.44}P values were generated by shifting InP n and κ data to the desired bandgap. Though the proposed tandem device structures are three dimensional, two dimensional simulations were employed as they maintain the features seen in three dimensional simulations with greatly reduced computational complexity, allowing for rapid cell design iteration.²⁵ The simulation cell bottom boundary was set to be perfectly reflecting, the sides were set to be periodic, and the top was designated to absorb all reflected light. Both TE and TM plane wave sources were used and the results for both polarizations were averaged. Previous experiments demonstrated

that coherent interface effects were suppressed in wires due to mild diameter tapering and small film variations and hence partial spectral averaging was employed to smooth this frequency specific resonances.³ Spectral averaging will also more closely represent the surface roughness evidenced in Fig. 2, again by smoothing the resonances. Finally, 200 spherical, 50 to 250 nm diameter, Al₂O₃ scattering particles were randomly distributed in the empty space to the sides of the wire to scatter light into the structure, and a 100 nm MgF, 60 nm TiO_x dual layer antireflective coating was placed over the outer Ga_{0.56}In_{0.44}P window. The antireflection coating was optimized to allow maximum transmission of the relevant wavelengths of the solar spectrum by using simple transfer matrix method calculations on a planar cell.

Device response to the solar spectrum was characterized by 23 optical simulations, stepped in 50 nm wavelengths throughout the AM1.5G solar spectrum.²⁵ The absorption was calculated independently in the Si_{0.1}Ge_{0.9}, in the GaAs_{0.9}P_{0.1}, and in the Ga_{0.56}In_{0.44}P by considering the real part of the divergence of the Poynting vector.²⁹ The optical generation was integrated over the volume and multiplied by the fundamental electric charge, yielding an assumed unity internal quantum efficiency J_{SC} . This procedure was repeated for all three geometries and for array pitches from $3\text{--}7 \mu\text{m}$ in $1 \mu\text{m}$ steps. For all of the simulations, the window layer was highly absorbing in the ultraviolet wavelengths and accounted for a loss of around $\sim 2 \text{ mA/cm}^2$ of all possible photocurrent.

The absorption in the conformal structure was relatively independent of wire pitch. Light incident between the wires scattered off of the Al₂O₃ particles and back into the array, allowing for high absorption regardless of packing fraction. The absorption profile, plotted in Fig. 6(b), for the full spectrum, revealed that light was directed into guided modes in the wire core, in contrast to the simple Beer-Lambert absorption assumed for the analytical model. As seen in Fig. 6(a), this facilitated high absorption in the infrared part of the solar spectrum despite the fact that $40 \mu\text{m}$ of Si_{0.1}Ge_{0.9} is not optically thick for these wavelengths. In the blue part of the spectrum, 500 nm of GaAs_{0.9}P_{0.1} absorbed $\sim 70\%$ of the incident photons, sufficient for current matching. Simple Beer Lambert absorption gives a slightly higher absorption rate of 74.5%, suggesting that the optical path length is not enhanced for the III–V layers in this structure. As the Si_{0.9}Ge_{0.9} wire core has a higher index than the GaAs_{0.9}P_{0.1} cladding, incoupled light is guided into the Si_{0.9}Ge_{0.9} core rather than residing in modes in the shell.

In contrast to the conformal structure, the hemisphere and sphere designs showed clear pitch dependence. While the Si_{0.1}Ge_{0.9} wire dimensions remained fixed for all cases, the hemisphere and sphere diameters scaled directly with the pitch in order to ensure that as much of the top surface as possible was screened by the III–V. For large wire array pitches, the III–V layers were optically thick and hence absorbed all of the blue light. Additionally, the III–V ellipsoids focused most of the red light onto the wire core where it was absorbed. However, light that reached the backside of the III–V in regions adjacent to the dielectric rather than the Si_{0.1}Ge_{0.9} wire was reflected out of the cell. Lowering the

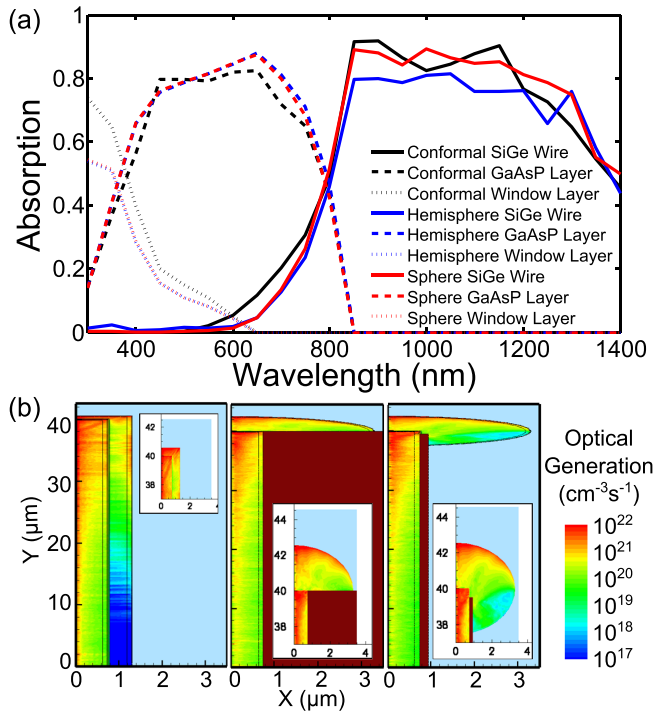


FIG. 6. Optical properties of multijunction wire arrays. (a) Absorption as a function of wavelength for the window, shell, and core layers and for all three structures. (b) The overall, AM1.5G, generation profile for the three structures at a 7 μm pitch. The plots are distorted laterally in order to encompass the full profile. The insets show an undistorted view of the top of the structures. The black lines denote the interface between the p-type and n-type regions of the top and bottom cells.

array pitch at fixed wire diameter led to thinner III–V layers which allowed the $\text{Si}_{0.1}\text{Ge}_{0.9}$ wire to absorb some of the blue light. The lower pitch also decreased the backside III–V/dielectric interfacial area, lowering reflection losses due to this interface. Current matched conditions were found for the 4 μm pitch. The spectral profile at this pitch is shown in Fig. 6(a).²⁵ Beer Lambert absorption for the 4 μm pitch structure suggests roughly equivalent absorption rates, again suggesting that the optical path length is not much altered.

For all structures, the current matched, idealized short circuit current densities were $\sim 21 \text{ mA/cm}^2$ in the wire and in the shell. To reach current densities closer to the theoretical maximum values, a series of graded index layers could be added on the back III–V/dielectric interface to couple red light out to the wire, longer wires could be used to allow

for greater absorption in the red, and window layers with higher bandgaps could be employed to mitigate parasitic absorption.

B. Device physics modeling

Next, the device physics properties of the 4 μm pitch, current matched structures were explored. The AM 1.5G optical photogeneration profile was utilized as data input in a drift-diffusion based device physics simulator (TCAD Sentaurus by Synopsys). Electronically, all three devices consisted of a base $\text{Si}_{0.1}\text{Ge}_{0.9}$ wire with a radial p–n junction, a highly doped $\text{Si}_{0.1}\text{Ge}_{0.9}/\text{Ga}_{0.56}\text{In}_{0.44}\text{P}$ tunnel junction and surface field, a $\text{GaAs}_{0.9}\text{P}_{0.1}$ p–n junction shell, and a $\text{Ga}_{0.56}\text{In}_{0.44}\text{P}$ front surface field. A representative band diagram is shown in Fig. 1. The electrical parameters of the materials were taken from the simulation database,³⁰ except for tunnel junction tunneling masses and effective Richardson constants which were taken from an AlGaAs/GaAs interface model.^{25,30} All interface recombination velocities were set to 100 cm/s for the initial simulations. The $\text{Si}_{0.1}\text{Ge}_{0.9}$ SRH lifetime was set to 1 μs ($L_n \sim 100 \mu\text{m}$), comparable to experimentally measured values,³ and SRH lifetimes of 1.25 ps, 5 ps, 20 ps, 500 ps, and 50 ns ($L_n \sim 157 \text{ nm}$, 315 nm, 629 nm, 3.15 μm , and 31.5 μm) were considered for the $\text{GaAs}_{0.9}\text{P}_{0.1}$. Auger and radiative recombination were also included. A small contact was located at the bottom center of the $\text{Si}_{0.1}\text{Ge}_{0.9}$ wire. The $\text{GaAs}_{0.9}\text{P}_{0.1}$ contact was either located at the outer base for the conformal structure or entirely covered the outside of the window layer for the hemisphere and sphere structures. Finally, cylindrical symmetry was specified, enabling the two-dimensional model to serve as a quasi-three-dimensional simulation.

First, tandem current-voltage curves were simulated. The efficiency, J_{SC} , and V_{OC} were extracted, and the results are plotted in Fig. 7. Maximum efficiencies of $\sim 22\%$ were found for all three cases at 50 ns $\text{GaAs}_{0.9}\text{P}_{0.1}$ lifetimes. As in the analytical model, when the diffusion length becomes comparable to the shell dimensions, a fraction of the generated carriers can no longer reach the junction before recombining, and the J_{SC} drops, becoming limited by the shell photocurrent. However, since the conformal structure features a uniform radial junction, the carrier pathlength for this geometry is shorter than the pathlength in the hemisphere or sphere structures. Thus, as the minority carrier lifetime

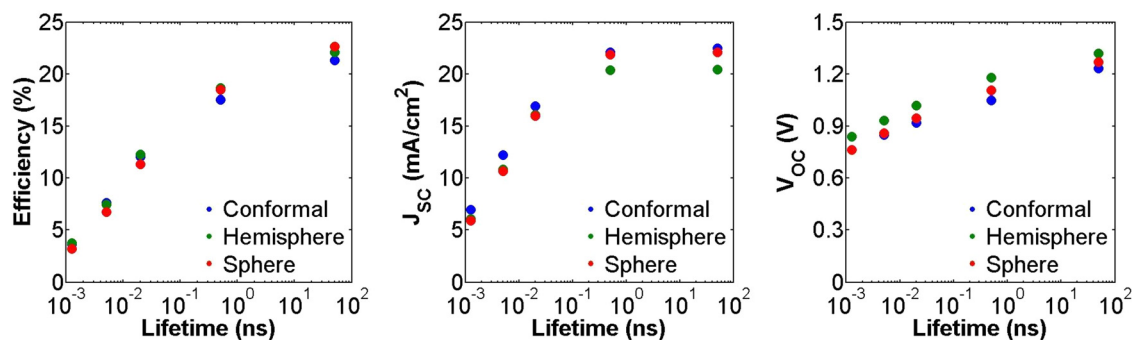


FIG. 7. Efficiency, short circuit current density, and open circuit voltage of the tandem wire array solar cell structures as a function of the $\text{GaAs}_{0.9}\text{P}_{0.1}$ SRH lifetime.

decreases, the J_{SC} in the conformal case remains higher than the J_{SC} for the other two cases.

The V_{OC} also falls with minority carrier lifetime for all of the structures. However, the decrease in V_{OC} for the hemisphere structure is slightly less than the decrease for the sphere which in turn is significantly less than the decrease for the conformal structure. This difference can be directly related to the difference in the overall volume of material for the three geometries. For example, for the $7\ \mu\text{m}$ pitch, the conformal structure contains $133.3\ \mu\text{m}^3$ of $\text{GaAs}_{0.9}\text{P}_{0.1}$, while the hemisphere contains only $57.5\ \mu\text{m}^3$ per wire. The larger defective volume leads to a higher dark current in the conformal structure and hence a lower V_{OC} .

In order to investigate the effects of the individual subcells, a contact was placed at the interface between the two cells, and each cell was simulated independently. The results from a representative hemispherical tandem structure with a 50 ns lifetime can be found in Table II. The simulation values compare favorably to the analytical values of Table I. The $\text{GaAs}_{0.9}\text{P}_{0.1}$ V_{OC} is lower in the simulation due to the addition of radiative and auger recombination and window layer resistance. The $\text{Si}_{0.1}\text{Ge}_{0.9}$ V_{OC} is also slightly lower due to Auger recombination and carrier transport along the length of the wire (the analytical model assumed that all transport in the wire was radial). As for J_{SC} , the $\text{GaAs}_{0.9}\text{P}_{0.1}$ current is smaller in the simulation due to reflection losses, while the $\text{Si}_{0.1}\text{Ge}_{0.9}$ current is appreciably lower due to the $40\ \mu\text{m}$ simulated wire length (limited to this value by computation memory). While the overall efficiency of the simulation is much reduced as compared with that of the analytical model, an increase in the $\text{Ga}_{0.1}\text{As}_{0.9}\text{P}$ V_{OC} through further optimization of the structure and doping profiles and an increase in the $\text{Si}_{0.1}\text{Ge}_{0.9}$ J_{SC} through the consideration of longer wires should bring the two values to convergence.

The effects of increasing the SRV on device performance were also explored. The $\text{Ga}_{0.56}\text{In}_{0.44}\text{P}$ surface, the $\text{Si}_{0.1}\text{Ge}_{0.9}/\text{Ga}_{0.56}\text{In}_{0.44}\text{P}$ interface, and the $\text{GaAs}_{0.9}\text{P}_{0.1}/\text{dielectric}$ interfaces of the sphere and hemisphere structures were given recombination velocities of first 10^4 and then $10^6\ \text{cm/s}$. The conformal structure was relatively insensitive to the SRV increase as the $\text{GaAs}_{0.9}\text{P}_{0.1}$ is uniformly coated with the $\text{Ga}_{0.56}\text{In}_{0.44}\text{P}$ window layer. The hemisphere and sphere, however, saw an appreciable drop in performance due to recombination at the $\text{GaAs}_{0.9}\text{P}_{0.1}/\text{dielectric}$ interfaces. Both had efficiencies $\sim 21\%$ at SRVs of $10^4\ \text{cm/s}$ and efficiencies of $\sim 17\%$ at $10^6\ \text{cm/s}$ (see Supplemental material²⁵).

Finally, in light of the work by Falub *et al.*,¹⁷ we also considered a modified hemispherical device in which a defective $\text{GaAs}_{0.9}\text{P}_{0.1}$ rectangular region was added below the

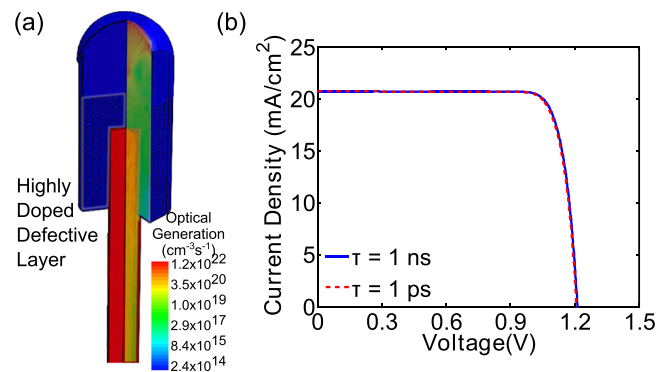


FIG. 8. The influence of a “defective” layer on device performance. (a) Optical generation profile and overview for a $\text{GaAs}_{0.9}\text{P}_{0.1}$ on $\text{Si}_{0.1}\text{Ge}_{0.9}$ cell with a “defective” layer. (b) Light IV curves for 1 ns and 1 ps SRH lifetimes in the “defective” layer.

hemisphere, as shown in Fig. 8(a). Falub *et al.* demonstrated that high quality material could be grown axially off of wires, leaving defects to propagate out radially from the growth interface. For our simulations, the upper $\text{GaAs}_{0.9}\text{P}_{0.1}$ hemisphere was set to have a lifetime of 1 ns. The lower defective $\text{GaAs}_{0.9}\text{P}_{0.1}$ region was set to have a high p-type doping concentration of 1×10^{19} in order to serve as a back surface field. The SRH lifetime in this region could be varied from 1 ns to 1 ps with only a 4 mV drop in V_{OC} and negligible change in J_{SC} , as shown in Fig. 8(b). The hemisphere is thick enough to absorb all of the above bandgap light and the high doping of the defective layer repels minority carriers away from the defective region and towards the junction. Thus, if defects due to lattice mismatch or polar on nonpolar growth can be grown out within a few microns of the wire base, the cell can achieve high efficiencies despite their presence.

IV. CONCLUSIONS

In conclusion, the feasibility, possibilities, and limitations of $\text{GaAs}_x\text{P}_{1-x}$ on $\text{Si}_{1-x}\text{Ge}_x$ tandem wire array multijunction solar cells have been demonstrated through masked GaAs on $\text{Si}_{0.9}\text{Ge}_{0.1}$ wire array growth and extensive modeling. We have shown that structures similar to the hemisphere and sphere designs can be successfully grown, and recent work suggests that these structures can have high material quality.¹⁷ An analytical model demonstrated that efficiencies approaching 34% should be possible with diffusion lengths on the order of $10\ \mu\text{m}$, optically thick materials, and a low loss tunnel junction. Full field optical modeling revealed that current matching can be realized with careful design and elucidates many of the reflection and absorption loss mechanisms, e.g., guiding into the wire and reflection of red light from the lower III-V/dielectric interface. Electronic modeling emphasized the importance of high lifetime material in the active layer, but suggested that defects at the heterointerface can have minimal impact if doped so as to repel minority carriers. Passivating the masking oxide/III-V interface will also be important for attaining high efficiencies. Finally, while we have specifically explored the implications of III-V on wire growth for creating tandem wire array cells, the mechanism may also be useful for creating flexible,

TABLE II. Light IV characteristics for a representative hemispherical tandem.

	V_{OC} (V)	J_{SC} (mA/cm ²)	Efficiency (%)	FF (%)
4 μm pitch $\text{GaAs}_{0.9}\text{P}_{0.1}$ shell	1.01	23.2	20.8	88.4
40 μm $\text{Si}_{0.1}\text{Ge}_{0.9}$ wire	0.26	20.0	3.58	67.7
Tandem	1.32	20.4	22.1	82.1

standalone III–V cells, LEDs, or other devices on a reusable Si wafer.

ACKNOWLEDGMENTS

We are grateful to Emily Warmann for assistance in detailed balance calculations, to Dr. Mike Kelzenberg and Dr. Mike Deceglie for their aid with Sentaurus, to Dr. Nick Strandwitz for helpful discussion, and to all of our teachers and family for their help and support through the years. Support for this work was provided by the United States Department of Energy under Grant No. DE-EE0005311. D.B.T-E. acknowledges the NSF for fellowship support.

- ¹E. Garnett and P. D. Yang, *Nano Lett.* **10**, 1082 (2010).
- ²M. D. Kelzenberg, S. W. Boettcher, J. A. Petykiewicz, D. B. Turner-Evans, M. C. Putnam, E. L. Warren, J. M. Spurgeon, R. M. Briggs, N. S. Lewis, and H. A. Atwater, *Nature Mater.* **9**, 329 (2010).
- ³M. D. Kelzenberg, D. B. Turner-Evans, M. C. Putnam, S. W. Boettcher, R. M. Briggs, J. Y. Baek, N. S. Lewis, and H. A. Atwater, *Energy Environ. Sci.* **4**, 866 (2011).
- ⁴M. C. Putnam, S. W. Boettcher, M. D. Kelzenberg, D. B. Turner-Evans, J. M. Spurgeon, E. L. Warren, R. M. Briggs, N. S. Lewis, and H. A. Atwater, *Energy Environ. Sci.* **3**, 1037 (2010).
- ⁵H. Goto, K. Nosaki, K. Tomioka, S. Hara, K. Hiruma, J. Motohisa, and T. Fukui, *Appl. Phys. Express* **2**, 035004 (2009).
- ⁶G. Mariani, P.-S. Wong, A. M. Katzenmeyer, F. Léonard, J. Shapiro, and D. L. Huffaker, *Nano Lett.* **11**, 2490 (2011).
- ⁷K. Cho, D. J. Ruebusch, M. H. Lee, J. H. Moon, A. C. Ford, R. Kapadia, K. Takei, O. Ergen, and A. Javey, *Appl. Phys. Lett.* **98**, 203101 (2011).
- ⁸Z. Fan, R. Kapadia, P. W. Leu, X. Zhang, Y.-L. Chueh, K. Takei, K. Yu, A. Jamshidi, A. A. Rathore, D. J. Ruebusch, M. Wu, and A. Javey, *Nano Lett.* **10**, 3823 (2010).
- ⁹L. Tsakalakos, J. Balch, J. Fronheiser, B. A. Korevaar, O. Sulima, and J. Rand, *Appl. Phys. Lett.* **91**, 233117 (2007).
- ¹⁰C. E. Kendrick, H. P. Yoon, Y. A. Yuwen, G. D. Barber, H. Shen, T. E. Mallouk, E. C. Dickey, T. S. Mayer, and J. M. Redwing, *Appl. Phys. Lett.* **97**, 143108 (2010).
- ¹¹Z. Fan, H. Razavi, J.-W. Do, A. Moriawaki, O. Ergen, Y.-L. Chueh, P. W. Leu, J. C. Ho, T. Takahashi, L. A. Reichertz, S. Neale, K. Yu, M. Wu, J. W. Ager, and A. Javey, *Nature Mater.* **8**, 648 (2009).
- ¹²J. Wallentin, N. Anttu, D. Asoli, M. Huffman, I. Åberg, M. H. Magnusson, G. Siefert, P. Fuss-Kailuweit, F. Dimroth, B. Witzigmann, H. Q. Xu, L. Samuelson, K. Deppert, and M. T. Borgström, *Science* **339**, 1057 (2013).
- ¹³K. E. Plass, M. A. Filler, J. M. Spurgeon, B. M. Kayes, S. Maldonado, B. S. Brunschwig, H. A. Atwater, and N. S. Lewis, *Adv. Mater.* **21**, 325 (2009).
- ¹⁴J. M. Spurgeon, K. E. Plass, B. M. Kayes, B. S. Brunschwig, H. A. Atwater, and N. S. Lewis, *Appl. Phys. Lett.* **93**, 032112 (2008).
- ¹⁵S. W. Boettcher, J. M. Spurgeon, M. C. Putnam, E. L. Warren, D. B. Turner-Evans, M. D. Kelzenberg, J. R. Maiolo, H. A. Atwater, and N. S. Lewis, *Science* **327**, 185 (2010).
- ¹⁶N. C. Strandwitz, D. B. Turner-Evans, A. C. Tamboli, C. T. Chen, H. A. Atwater, and N. S. Lewis, *Adv. Energy Mater.* **2**, 1109 (2012).
- ¹⁷C. V. Falub, H. von Känel, F. Isa, R. Bergamaschini, A. Marzegalli, D. Chrastina, G. Isella, E. Müller, P. Niedermann, and L. Miglio, *Science* **335**, 1330 (2012).
- ¹⁸K. K. Lew, L. Pan, E. C. Dickey, and J. M. Redwing, *Adv. Mater.* **15**, 2073 (2003).
- ¹⁹E. I. Givargizov, *J. Cryst. Growth* **20**, 217 (1973).
- ²⁰B. M. Kayes, M. A. Filler, M. C. Putnam, M. D. Kelzenberg, N. S. Lewis, and H. A. Atwater, *Appl. Phys. Lett.* **91**, 103110 (2007).
- ²¹B. M. Kayes, H. A. Atwater, and N. S. Lewis, *J. Appl. Phys.* **97**, 114302 (2005).
- ²²J. Humlicek, in *Handbook of Optical Constants of Solids*, edited by E. D. Palik (Elsevier, 1998), Vol. III, Part II, Chap. 22.
- ²³The Ioffe Institute (Ioffe Institute, St. Petersburg, 2001), Vol. 2012, see <http://www.ioffe.rssi.ru/SVA/NSM/Semicond/>.
- ²⁴C. F. Bohren and D. R. Huffman, *Absorption and Scattering of Light by Small Particles* (John Wiley & Sons, New York, 2004).
- ²⁵See supplementary material at <http://dx.doi.org/10.1063/1.4812397> for more information and a plot comparing the Mie theory and Beer Lambert absorption; further discussion of the effect of increasing the SRV; further analysis of series resistance effects; further comparison of two dimensional vs. three dimensional simulations; a comparison between the course and fine simulations; a summary of the optical absorption and loss mechanisms and further discussion of the pitch dependence; and more information of the specific parameters.
- ²⁶R. L.-Y. Sah, R. N. Noyce, and W. Shockley, *Proc. IRE* **45**, 1228 (1957).
- ²⁷M. T. Sheldon, C. N. Eisler, and H. A. Atwater, *Adv. Energy Mater.* **2**, 339 (2012).
- ²⁸See <http://www.lumerical.com> for more information on the software.
- ²⁹V. E. Ferry, L. A. Sweatlock, D. Pacifici, and H. A. Atwater, *Nano Lett.* **8**, 4391 (2008).
- ³⁰See <http://www.synopsys.com> for more information on the software.